Lattice preferred orientation and seismic anisotropy in sedimentary rocks

S. L. A. Valcke,[1,*] M. Casey,[1] G. E. Lloyd,[1] J.-M. Kendall[1,†] and Q. J. Fisher[1,2]

[1]*School of Earth Sciences, University of Leeds, Leeds* LS2 9JT, *UK. E-mail: valcke@geo.uu.nl*
[2]*Rock Deformation Research, University of Leeds, Leeds* LS2 9JT, *UK*

SUMMARY

Although it is well known that sedimentary rocks can be seismically anisotropic, there have been few detailed investigations of the underlying cause of such anisotropy. Here, we investigate anisotropy due to the preferred orientation of minerals, or lattice preferred orientation (LPO), in a suite of sedimentary rocks. Seismic properties are predicted by averaging single-crystal elastic constants of minerals according to their crystal orientation and modal volume fraction in the rock aggregate. Both Electron Backscattered Diffraction (EBSD) and X-ray Texture Goniometry (XTG) are tested as quantitative techniques for measuring the LPO of sedimentary rocks. Although EBSD has promise for future LPO measurements in polymineralic sedimentary rocks, problems currently remain in measuring low-symmetry phases (e.g. feldspars) and very small clay or mica particles. However, the LPO of very fine-grained phyllosilicates can be measured using XTG and the LPO of low-symmetry minerals can be measured using manual EBSD pattern analysis. Here, we use such a hybrid approach to estimate LPO in a suite of sedimentary samples. The seismic properties calculated from LPO data show anisotropy values for *P*-waves ranging from 1.5 per cent in sandstones, to over 3.5 per cent in a siltstone, to 12 per cent in a shale. The effect of thin multilayering on long-wavelength propagation in a siltstone is predicted by applying Backus-type averaging. The layering does not enhance the anisotropy because of the small differences in density and in elasticity between the two layer types. The LPO of phyllosilicates and to a lesser extent dolomite and siderite seem to contribute significantly to the seismic anisotropy of phyllosilicate-rich rocks (siltstones and shales). The weak LPO of quartz in sandstones causes a few per cent anisotropy. Cumulatively, our results suggest that field observations of seismic anisotropy have the potential to be used as an indicator of rock lithology.

Key words: crystallography, exploration seismology, mineralogy, sediments, seismic anisotropy, seismic velocities, shear-wave splitting.

1 INTRODUCTION

Seismic anisotropy refers to a change in wave velocity and polarization with propagation direction. It can be caused by a variety of factors, from the large scale (e.g. aligned faults, layering) to the small scale (e.g. aligned cracks and crystals). It is well known that the small-scale, or microstructural, factors include (e.g. Kern & Wenk 1985; Mainprice *et al.* 2003): (1) crystal lattice preferred orientation (LPO) of constituent mineral phases; (2) variations in spatial distribution of grains and minerals; (3) grain morphology [e.g. shape and

dimensional preferred orientation (SPO)]; and (4) aligned fractures, cracks and pores, and the nature of their infilling material (e.g. clays, hydrocarbons, water, etc.). Because of the overall microstructural control on seismic anisotropy, it follows that anisotropy can be diagnostic for specific rock types. Here, we consider whether seismic anisotropy can be used as an indicator of specific sedimentological lithologies within the Earth's crust.

The contribution to the overall anisotropy in sedimentary rock from each of the four causes mentioned above is not well understood. So, before the factors can be considered simultaneously, their individual effects on seismic anisotropy still need to be investigated separately. Here, we concentrate on the contribution from LPO, an effect that has received little previous attention. We develop a methodology for estimating LPO-related seismic anisotropy in sedimentary rocks using microstructural analyses and apply it to a suite of typical sedimentary rocks.

*Now at: Faculty of Geosciences, Utrecht University, PO Box 80.021, 3508 TA Utrecht, the Netherlands.

†Now At: Department of Earth Sciences, University of Bristol, Bristol BS8 1RJ, UK.

Until recently, the complexity of the Earth's heterogeneous crust, particularly when compared to the lithospheric mantle, has made it difficult to justify assumptions of continuous microstructural elements on the scale of seismic wavelengths. However, progress in the resolution of controlled source seismic exploration and processing techniques makes it now worthwhile to investigate any link between microstructural observations and seismic data in crustal rocks (e.g. Carlson *et al.* 1984; Mainprice & Nicolas 1989; Lloyd & Kendall 2005). Nevertheless, very few quantitative anisotropy studies on sedimentary rocks have been performed (e.g. Jones & Wang 1981; Hornby 1998).

Most studies of seismic anisotropy in sedimentary rocks have concentrated on shales, using either theoretical studies of the effect of LPO or ultrasonic measurements (e.g. MacDonal *et al.* 1958; Kaarsberg 1959; Jones & Wang 1981; Tosaya & Nur 1982; Banik 1984; Vernik & Nur 1992; Hrouda *et al.* 1993; Hornby *et al.* 1994; Sayers 1994; Johnston & Christensen 1995). The definition of LPO in shales has been restricted to phyllosilicate minerals and has been qualitative rather than quantitative. However, other minerals also occur in shales (e.g. quartz) and their orientation can alter the overall LPO-induced seismic anisotropy. The intrinsic seismic anisotropy for sedimentary rocks other than shales has been estimated only via ultrasonic measurements (Carlson *et al.* 1984; Wang 2002). No quantitative links have been made between seismic anisotropy in sandstones or carbonates and the LPO of their constituent minerals. Wang (2002) mentioned the possible effect of clay content, but it is neglected because of the low anisotropy values. Although seismic anisotropy values for sedimentary rocks can be indeed low, they remain sufficient to be extracted from seismic data (e.g. Alkhalifah & Rampton 2001).

Furthermore, ultrasonic measurements often assume vertical transverse isotropy (VTI) (hexagonal symmetry with a vertical symmetry axis) and in general three or four measurement directions are chosen according to this symmetry. Unfortunately, there are insufficient studies of the causes of intrinsic anisotropy, particularly in sandstones and carbonates, to assume only VTI symmetry. If sedimentary rocks have a different symmetry, any seismic anisotropy based on an assumption of VTI may be erroneous. The approach in this study is first to measure the LPO of each mineral phase in three sedimentary rock types (shale, sandstone and siltstone) and then to calculate seismic velocities in all directions based on the LPO. From the velocities, seismic anisotropy can be predicted for any direction without assuming VTI. This study not only provides insights into the LPO of minerals in sedimentary rocks, but also provides a helpful methodology for future predictions of seismic anisotropy in sedimentary rocks. This, in turn, will lead to a better understanding and better processing of seismic data from sedimentary basins.

2 METHODOLOGY

2.1 Motivation for methodology

Before rock properties and lithologies can be inferred from seismic data, it is important to know the relative contribution of each factor that might induce seismic anisotropy. Current understanding of how microstructural variables influence seismic anisotropy is based mainly on ultrasonic measurements (e.g. Peselnick *et al.* 1974; Vernik & Nur 1992; Kern 1993; Lee & Alexander 1995; Dewhurst *et al.* 2002; Wang 2002; Herwanger *et al.* 2004) and on theoretical models in which microstructural variables are incorporated (e.g. Ponte Castaneda & Willis 1995; Thomsen 1995;

Blackman *et al.* 1996; Hornby 1998; Jakobsen & Johansen 2000; Tommasi *et al.* 2000; Wendt *et al.* 2003). Both approaches have limitations. In ultrasonic measurements, the bulk seismic anisotropy of the aggregate is measured and it is difficult to separate the contribution of each individual microstructural factor. Theoretical models are limited by boundary conditions and, although they tend to be very complex, at present cannot include all microstructural factors that might contribute to seismic anisotropy. Thus, for the moment it seems useful to investigate each variable separately. Here, we study the effect of LPO alone on seismic wave velocities, a microstructural control that has been recognized since the late 1950s (Kaarsberg 1959; Hess 1964; see also Babuska & Cara 1991).

In a rock aggregate, each mineral component contributes to the overall seismic anisotropy of the aggregate according to its elastic properties (i.e. single-crystal anisotropy), bulk LPO and volume fraction. In particular, the impact of LPO depends strongly on how the single-crystal fast and slow seismic velocity directions are oriented in relation to the crystal axes. Most LPO-causing mechanisms considered in seismic anisotropy studies are induced by tectonic strain in highly deformed rocks (e.g. Babuska & Cara 1991; Blackman *et al.* 1996). When relating LPO to seismic anisotropy in sedimentary rocks, the LPO-causing mechanisms that mostly have been mentioned to date are gravitational and mechanical compaction. Detrital grains that can exhibit LPO due to these mechanisms tend to have elongate or platy shapes that are closely related to the mineral crystal structure (e.g. clay and phyllosilicate minerals). Sedimentological studies have shown that there are mechanisms other than gravitational deposition and mechanical compaction that might cause LPO to develop, such as diagenetic growth of minerals (e.g. Archibald *et al.* 1996) or a strong current during deposition of elongate minerals (Pettijohn 1975).

It follows therefore that in order to predict seismic anisotropy accurately, a quantification of the LPO of each mineral phase is needed, which to date rarely has been obtained in sedimentary rocks. In this study, two quantitative techniques have been used to investigate the LPO. The first technique is Electron Backscattered Diffraction (EBSD) using the Scanning Electron Microscope (SEM) and the second technique is X-ray Texture Goniometry (XTG). Once the LPO and modal mineralogy of a sample have been defined, the average elastic properties and seismic velocities are calculated from the LPO and volume fractions of each mineral phase using the Hill principle (Hill 1952). To see whether layering (e.g. bedding) is an important feature on the scale of the sample, its influence on long-wavelength seismic anisotropy is modelled using a Backus approach (Backus 1962).

2.2 Microstructural analysis

Full LPO analysis in 3-D is now possible via SEM-EBSD (e.g. Prior *et al.* 1999). Although SEM-EBSD is well established in the study of crystalline rocks, this study applies for the first time EBSD to determine the LPO of sedimentary rocks.

2.2.1 SEM EBSD

SEM-EBSD provides the mineral phase and the precise crystallographic orientation of a grain at the point of incidence of the electron beam on the sample surface with a spatial resolution of ∼1 μm and angular resolution of ∼1° (see Prior *et al.* 1999; Humpreys 2001, for details). This study used the HKL Channel 5 package (Schmidt & Olesen 1989) to define the crystal orientation from diffraction patterns. In automated EBSD analyses, the large data sets

Table 1. Summary of SEM EBSD experimental details. See text for details.

Sample	Mineralogy	Average grain area	Step-size (μm)	Average steps per grain	Number of grains	Indexed points (per cent)	Average MAD	Success per phase (per cent)
SV1	Quartz	2500 μm^2	5	100	936	26	0.61	67
6 mm^2	Dolomite	1000 μm^2	5	40	600	7	0.69	70
	K-feldspar	1000 μm^2	5	40	300	4	0.74	80
	Mica (Mus, Bio, Ill)	500 μm^2	5	20	720	7	0.91	117
	Chlorite	500 μm^2	5	20	600	1	0.96	20
	Kaolinite	–	–	–	–	0	–	–
	Siderite	30 μm^2	Manual	2	400	Manual	–	100
	Pyrite	–	–	–	–	0	–	–
	Total indexing	–	–	–	–	45	–	–
SV2	Quartz	500 μm^2	5	20	3360	10	0.75	36
6 mm^2	K-feldspar	500 μm^2	5	20	600	5	0.80	156
	Albite	–	–	–	–	0	–	–
	Pyrite	–	–	–	–	0	–	–
	Muscovite/Biotite	300 μm^2	5	12	2600	7	0.98	55
	Illite	–	–	–	–	0	–	–
	Kaolinite	–	–	–	–	0	–	–
	Chlorite	–	–	–	–	0	–	–
	Total indexing	–	–	–	–	22	–	–
SV6	Quartz	0.05 mm^2	25	160	2000	38	0.64	64
1, 44 cm^2	K-feldspar	–	–	–	–	0	–	–
	Kaolinite	–	–	–	–	0	–	–
	Total indexing	–	–	–	–	38	–	–
SV7	Quartz	0.06-0.6 mm^2	25	96	1000	33	0.73	45
1, 2 cm^2	Albite	–	–	–	–	0	–	–
	Kaolinite	–	–	–	–	0	–	–
	Illite	–	–	–	–	0	–	–
	Total indexing	–	–	–	–	33	–	–
SV8	Quartz	0.1–20 mm^2	15	444	600	30	0.69	48
1, 1 cm^2	Albite	–	–	–	–	0	–	–
	Kaolinite	–	–	–	–	0	–	–
	Illite	–	–	–	–	0	–	–
	Total indexing	–	–	–	–	30	–	–

necessary for determining the near-random LPO, potentially common in sedimentary rocks, can now be obtained.

Because SEM-EBSD is used for the first time on sedimentary rocks in this study, appropriate sampling strategies had to be established. As a general rule, the largest possible specimen area should be sampled. In particular, for samples with weak LPO a minimum of 1000 grains should be measured. Also, a sufficiently small step size is required, so that 15–45 points are measured per average grain size. This constraint is mainly to remove isolated data points that have been indexed incorrectly. Consequently, appropriate sampling strategies differed from sample to sample and are summarized in Table 1.

Although EBSD indexing is known to be reliable for many minerals, such as quartz, dolomite and calcite (e.g. Prior *et al.* 1999), it can be unreliable for phyllosilicates and feldspars, which often yield poor-quality (e.g. due to specimen preparation problems) and/or complex EBSD patterns (e.g. due to low crystal symmetry). XTG is a well-established, alternative technique for the measurement of the *c*-axes of mica and clay minerals. Unfortunately, it cannot be used to measure feldspars, which therefore had to be indexed via manual EBSD analysis. Siderite and pyrite have a high Fe content, resulting in EBSD patterns with high background contrast. Such high-contrast minerals typically also have to be indexed manually after an appropriate background subtraction, although recent developments in EBSD technology should alleviate this problem.

EBSD pattern indexing is achieved via comparison between observed and expected pattern configurations, with the latter selected

from a predefined database for each mineral (e.g. Prior *et al.* 1999). The measure of comparison used is the mean angular deviation (MAD) between the two pattern configurations, which we set to be smaller than 1.0°, in accordance with conventional practice to have reliable indexing (see Table 1). An estimate of the success rate for indexing each mineral can be determined by comparing the percentage of indexed points to the modal percentage of the mineral (Table 1) and typically varies from mineral to mineral and sample to sample. In the siltstone and sandstones, indexing success rates for quartz vary from 48 to 67 per cent. These relatively low values are due to the high porosity of these rocks, which causes local charging and a denigration of EBSD pattern quality at grain edges. The shale and slate have an average indexing success for quartz of only ∼33 per cent due to the small grain size, which causes a greater probability of the incident electron beam striking grain boundaries resulting in poor pattern quality. The indexing problems associated with phyllosilicates and feldspars mentioned above often lead to false modal estimates (i.e. chlorite indexed as muscovite, or muscovite indexed as feldspar, etc.) and may cause 'success/phase values' to exceed 100 per cent (see Table 1). For this reason, the orientations of these minerals were determined via either manual EBSD or XTG methods (see below).

2.2.2 X-ray texture goniometry

The main difference between EBSD and XTG (see Cullity 1978, or van der Pluijm *et al.* 1994, for general overview of XTG) is

that the latter measures only the bulk aggregate LPO for a particular mineral, whilst EBSD produces point measurements that can be related directly to position and hence specific individual minerals. XTG analyses were performed for: (1) muscovite + biotite + illite; and (2) chlorite + kaolinite. Although XTG analysis of chlorite and kaolinite can be problematic due to the broadening of diffraction peaks by random clay minerals, adaptations of the basic March model (March 1932; Means *et al.* 1984) offer a viable solution. According to this model, plate-shaped detrital grains reorient in the same way under similar stress conditions (e.g. compaction). Thus, for the same sample, the LPO of each detrital phyllosilicate mineral normalized over the modal proportion of that mineral should be comparable.

Because XTG data have been obtained only for the *c*-axes of phyllosilicate minerals, the full 3-D orientation of the crystals is not defined. Assumptions need to be made therefore to produce the 3-D orientation distribution function (ODF) necessary for the seismic predictions. In a typical sedimentary rock, phyllosilicate *c*-axes are most likely to occur normal to bedding, with the *a*- and *b*-axes randomly oriented within the bedding (e.g. Kaarsberg 1959; Hornby 1998). In this study, this typical configuration is assumed, in which case it is sufficient to perform XTG transmission scans of the *c*-axes on layer normal sections and to impose radial symmetry to calculate the ODF (e.g. Casey 1981).

2.3 Mineralogical analysis

To predict the elastic properties of rock, it is important to quantify not only the LPO of the constituent minerals, but also their modal proportion. The misindexing associated with low-symmetry minerals and the often small grain-sizes made EBSD determination of modal proportions unreliable. Instead, two alternative approaches were used: (1) image analysis of backscattered electron (BSE) atomic number (*Z*) contrast photomicrographs (sandstone samples); and (2) quantitative X-ray diffraction (QXRD) (shale and siltstone samples) (Hillier 1999, 2000).

2.4 Prediction of seismic properties

2.4.1 LPO

The seismic properties of rock aggregates are predicted first by calculating the elastic properties of the aggregate and secondly by relating the elasticity to the seismic velocities in 3-D. The aggregate elastic properties are derived by rotating the single-crystal elastic tensor for each mineral phase into the sample reference frame according to its LPO characteristics and to calculate the bulk elastic

tensor for that phase. Next, the aggregate elastic tensor is found by averaging the rotated elastic tensors of each mineral phase according to their modal fractions. Both the orientation and volume averaging are achieved using the Voigt–Reuss–Hill (VRH) principle (Voigt 1928; Reuss 1929; Hill 1952). It has been suggested that the closest approximation to ultrasonic measurements of seismic properties is provided by the Voigt average (e.g. Peselnick *et al.* 1974; Seront *et al.* 1993). However, this has been demonstrated only for highly deformed rocks with specific textures. It is not known which average is most appropriate for sedimentary rocks. Until there is more evidence for the appropriate averaging scheme, it seems most appropriate to adopt the Hill average (Hill 1952), which is the arithmetic mean of the Voigt and Reuss values.

The next step is to calculate the seismic velocities in 3-D from the Hill averaged aggregate elastic tensor (C_{ijkl}). This is achieved via the Christoffel equation (e.g. Babuska & Cara 1991):

$$\det \left| C_{ijkl} X_i X_j - \delta_{kl} \rho V^2 \right| = 0, \tag{1}$$

in which X_i is the wave front normal, δ_{kl} is the Kronecker delta, ρ the density and V the phase velocity of a seismic wave in the given direction. Due to the symmetry of the stress and strain tensor, elasticity can be expressed by C_{ij} coefficients (GPa) in a symmetric 6×6 matrix. The calculation of the aggregate elasticity is performed simultaneously with the calculation of seismic velocities using the FORTRAN program, *Anis2Ck* (Mainprice 1990), subsequently adjusted for both individual Euler angles (EBSD) and ODF functions (XTG) as the input data. The velocity calculations are performed in all directions and presented as 2-D pole figures. Note that in this method of calculating seismic properties, only the anisotropy effect of LPO is considered by simulating an aggregate having the same modal mineralogy of the samples, but containing neither pores nor cracks. Consequently, predicted seismic velocities are unnaturally high due to the high density of such a simulated aggregate. Incorporating porosity would lower the seismic velocities to more realistic values. However, an approximation of the effect of porosity has not been made as this is beyond the scope of this study (see above) and because the original amount and shape of the pores before the drilling of the samples is not known.

The single-crystal data (density and elasticity) used in this study are listed in Table 2. The elasticity data are for room temperature and atmospheric pressures because pressure–temperature derivatives of the sedimentary minerals are currently not available and it is likely that elasticity pressure–temperature dependence of sedimentary minerals does not affect the seismic anisotropy at shallow basin depths (see Mainprice *et al.* 2000; Blackman & Kendall 2002, for more details). When muscovite, biotite and illite could not be separately measured, the elasticity of the three minerals is calculated

Table 2. Summary of single-crystal-density and elastic-property data used in this study.

Mineral	Density	Elasticity data (10^{-3} kg m^{-3})
Quartz	2.66	Quartz (McSkimin *et al.* 1965)
Dolomite	2.86	Dolomite (Bass 1995)
K-feldspar	2.54	Orthoclase (Landolt-Bornstein 1984)
Albite	2.64	Albite (Bass 1995)
Muscovite, biotite, illite	∼2.88	Muscovite (Vaughan & Guggenheim 1986)
Chlorite	2.70	Chlorite (Katahara 1996)
Kaolinite	2.52	Kaolinite (Katahara 1996)
Illite	2.79	Illite (Katahara 1996)
Siderite	3.90	Rhodochrosite (Chen *et al.* 2001)
Pyrite	5.00	Pyrite (Bass 1995)

from the muscovite elasticity (sample SV1 and SV2). As there appear to be no elasticity data available for siderite, the single-crystal elasticity of rhodochrosite has been used as the structure and composition of both minerals are similar.

The *P*-wave anisotropy parameter (AV_P) used in this study, is a function of the maximum ($V_{P,\max}$) and minimum ($V_{P,\min}$) velocities:

$$AV_P = 100 \left[\frac{(V_{P,\max} - V_{P,\min})}{0.5\,(V_{P,\max} + V_{P,\min})} \right]. \tag{2}$$

The *S*-wave splitting parameter (AV_S) is a function of the maximum ($V_{s1,\max}$) and minimum ($V_{s2,\min}$) shear wave velocities in a given direction:

$$AV_S = 100 \left[\frac{(V_{s1,\max} - V_{s2,\min})}{0.5\,(V_{s1,\max} + V_{s2,\min})} \right]. \tag{3}$$

2.4.2 Layering

In addition to LPO, it is known that periodic thin layering may influence also aggregate seismic properties (Backus 1962). Our calculations are based on long-wavelength 'Backus averaging', except that intrinsically anisotropic layers are considered (e.g. Schoenberg & Muir 1989). The general principle of this approach is that an equation is found to relate the strain in one layer to the strain in an adjacent layer. From this relationship, the strain in both layers can be found from the condition that the individual layer strains must sum to the imposed strain according to the layer thicknesses. Once the layer strains have been found, the corresponding layer stresses can be determined and, hence, the bulk stress can be derived. The elastic tensor can then be calculated from the strains and stresses via Hooke's law.

Backus-style averaging applies to any length-scale as long as the thicknesses are smaller than the seismic wavelength. This is, for example, the case for the microlayered siltstone SV1. However, care should be taken as the scale of the layering may change laterally or vertically. Also, Backus-style averaging cannot be used to compare seismic predictions with ultrasonic measurements. The latter involve millimetre-scale wavelengths that approach the microlayer thickness and are sensitive therefore to dispersion and reflection effects. Unfortunately, there are no easily applicable short-wavelength approximations currently available that could calculate the full effective elastic tensor.

2.5 Reference frames and data presentation

A precise sample reference frame is required if the predictions of seismic anisotropy via LPO are to be compared with other samples or with seismic field data from the area. In the samples considered in this study, bedding is (sub)horizontal and the core axis is vertical (direction of Y_s-axis in Fig. 1a), so the core axis is (sub)normal to the bedding plane. Samples were prepared therefore in the following orientations (Fig. 1a): (1) parallel to core axis and normal to dip of bedding plane; (2) parallel to core axis and parallel to dip of bedding plane; or (3) parallel to the bedding plane.

The reference frame for the LPO and seismic data and their relationship with the layering and EBSD acquisition surface are shown on Fig. 1(a). Both the LPO data and seismic velocities are presented on pole figures showing contour lines of equal-area, upper-hemisphere projections of 3-D data, using software written by Mainprice (1990). Wenk (1985) provided details on the projection techniques and interpretation of pole figures. The contour lines on
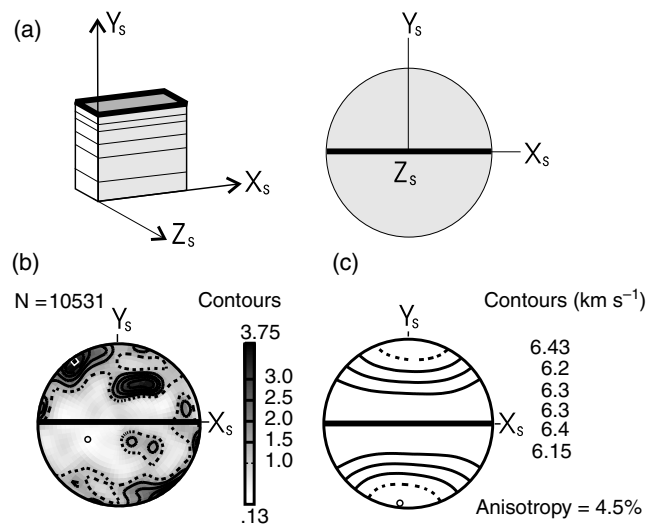

Figure 1. (a) Definition of reference frames for sedimentary samples, LPO and seismic properties. (b) LPO pole figure of dolomite (data points: $n = 10\,531$) on which the distribution of the normal to the lattice plane ($h\,k\,l$) is shown; in this case the *c*-axis normal to (0 0 1). (c) Pole figure for seismic *P*-waves showing the trend of velocity contour lines and an overall anisotropy of 4.5 per cent. In (a), (b) and (c), the orientation of layering in the sample is indicated by the thick black line.

the LPO pole figures are density contours of crystal orientations, expressed as multiples of the uniform (i.e. spherical random) distribution (m.u.d.) (Fig. 1b). The m.u.d. value represents the strength of a single axis orientation distribution and not of the whole LPO. The contour lines on the pole figures of seismic properties are velocity contours in km s^{-1} (Fig. 1c). The LPO and seismic data pole figures are represented such that the core axis (direction of Y_s-axis) is vertical and the projection of the layering appears as a horizontal or dipping line through the centre of the pole figure (Fig. 1). For clarity, the layering is indicated by a thick black line on all pole figures. The reference frame of the elasticity matrices is such that C_{33} is in the direction parallel to the core axis (direction of Y_s-axis), so normal to the layering, except for SV8.

3 SPECIMEN DETAILS

The samples are sedimentary rocks from either the Halten Terrace or Viking Graben in the North Sea. All rocks are middle Jurassic in age and come from depths between 2.5 and 4 km. Modal mineralogy and porosity data are given in Table 3.

3.1 SV1—siltstone

Siltstone SV1 consists of alternating 1–8 mm thick layers that have two distinct lithologies: dark mud rich and light sand rich (Fig. 2a and Table 3). In the mud-rich layers, a clear bedding-parallel shape fabric is visible due to the alignment of detrital phyllosilicates and also aligned authigenic clays where they have replaced detrital phyllosilicates, which represents about one-third of the clay minerals (Fig. 2b). The rest of the authigenic clays (~70 per cent) have filled pore space and they tend to be randomly oriented. Quartz, K-feldspar and dolomite are ellipsoidal to equant and do not define a clear shape fabric. Diagenetic siderite minerals have rhombohedral shapes and are ~50 per cent aligned parallel to mica (Fig. 2c) and ~50 per cent randomly oriented (Fig. 2d), whilst diagenetic pyrite is framboidal

Table 3. Porosity (per cent) (not included in the seismic predictions); modal mineralogies and densities (both excluding porosity) used for the seismic predictions; and seismic anisotropy (per cent) of analysed samples. For siltstone SV1, the illite percentage is included in the mica percentage as both could not be measured separately. Porosity was measured using image analysis, mercury-injection or He-porosimetry.

Modal mineralogy (per cent) (excluding porosity)	Silt SV1 Mud-rich (63 per cent)	Silt SV1 Sand-rich (37 per cent)	Shale SV2	Sandstone SV6	Sandstone SV7	Sandstone SV8
Quartz	37.1	48.2	28.1	83.1	89.2	84.0
Dolomite	1.9	20.8	–	–	–	–
K-feldspar	5.8	4.7	3.2	15.5	–	–
Albite	–	–	1.3	–	4.8	9.4
Mica (muscovite, biotite, illite)	8.7	3.9	29.3	–	–	–
Chlorite	7.3	3.0	6.6	–	–	–
Kaolinite	27.0	15.6	30.3	1.4	3.6	5.3
Illite	–	–	–	–	2.4	1.3
Siderite	10.2	2.8	–	–	–	–
Pyrite	2.0	1.0	1.2	–	–	–
Bulk porosity (per cent)	10[a]		<1	29	17	25
Bulk density (excluding porosity) (10^{-3} kg m^{-3})	2.82	2.79[a]	2.71	2.64	2.66	2.65
P-wave anisotropy (per cent)	4.5	3.4 ... 3.7[a]	11.1	1.5	2.6	2.1
Maximum *S*-wave splitting (per cent)	3.7	3.0 ... 3.1[a]	9.8	1.4	3.1	2.5

[a]Data for layer stack of SV1.

and does not show any obvious relation to the bedding-parallel fabric. The sand-rich layers do not show an obvious bedding-parallel fabric as they contain less phyllosilicates and authigenic clays are ~90 per cent pore-filling with random orientations (Fig. 2e). There are some bedding-parallel cracks, especially in the phyllosilicate-rich parts, which probably formed as a result of exhumation-related stress relaxation.

3.2 SV2—shale

Shale SV2 exhibits no mineralogical layering, although a bedding-parallel shape fabric due to alignment of phyllosilicates is visible (Fig. 2f). Most authigenic clays have an alignment as they have replaced the abundant detrital mica and chlorite, rather than precipitating randomly in pores. Quartz and feldspar grains are common and have equant shapes. There are rare concentrations of randomly oriented framboidal pyrite, whilst organic material forms subspherical to ellipsoidal patches of 30–50 µm size. Bedding-parallel cracks are also present, probably due to stress relaxation (Fig. 2f).

3.3 SV6—sandstone

Sandstone SV6 is moderately to well sorted and fine grained (Fig. 2g). It has experienced a relatively shallow burial of 2600 m. The macroscopic layering is horizontal but cannot be seen microscopically. Most quartz grains exhibit irregular boundaries due to diagenetic grain–grain contact dissolution, which has provided the source for the minor authigenic quartz overgrowths. Feldspar grains also show diagenetic overgrowths. Kaolinite is mainly randomly oriented in the occluded pore space.

3.4 SV7—sandstone

Sandstone SV7 is moderately sorted and medium grained (Fig. 2h). It has experienced a relatively deep burial of 3800 m. The macroscopic layering is horizontal but cannot be seen microscopically. In contrast to sample SV6, there is a significant amount of diagenetic quartz overgrowths.

3.5 SV8—sandstone

Sandstone SV8 is moderately sorted and coarse grained (Fig. 2i). It has experienced a relatively deep burial of 3800 m. The macroscopic layering dips 30° and is visible also on the microscopic scale as the alignment of larger, elongate quartz grains. The amount of diagenetic quartz in this sample is similar to SV7. The clays are mainly randomly oriented in the pore spaces.

4 RESULTS

4.1 Measured LPO analyses

4.1.1 SV1—siltstone (Fig. 3)

The quartz LPO is near random, with the maximum m.u.d. varying between 1.36 and 1.78. These are the lowest values compared to other minerals in the sample. However, the quartz *c*-axes show a slight preferred orientation in a girdle subparallel to bedding, with a tendency for alignment at 20° from the bedding plane, whilst *m*-poles and *a*-axes are subnormal to bedding. The dolomite LPO has higher maximum m.u.d. values (1.94–3.75). The *c*-axes form the strongest concentrations, at 30°–40° from the bedding plane normal, whilst the *a*-axes and *m*-poles define girdles oblique to bedding. The XTG LPO analysis of chlorite and kaolinite showed severe diffraction peak broadening due to a substantial proportion of randomly oriented, authigenic kaolinite. However, the XTG LPO analysis of biotite, muscovite and illite did not suffer from diffraction peak broadening as the majority of authigenic illite is aligned and adds to any diffraction peaks. Fortunately, the proportions of aligned kaolinite in the mud-rich layers and sand-rich layers could be estimated at ~30 and ~10 per cent, respectively, via BSE imaging. The LPO of aligned kaolinite and chlorite fractions can be described by the muscovite and biotite analysis, as explained in the methodology. The overall mica-clay LPO shows a relatively strong concentration of *c*-axes perpendicular to bedding. The remaining kaolinite fraction is described by a random ODF. Siderite was analysed manually and considered both random and aligned siderite concentrations
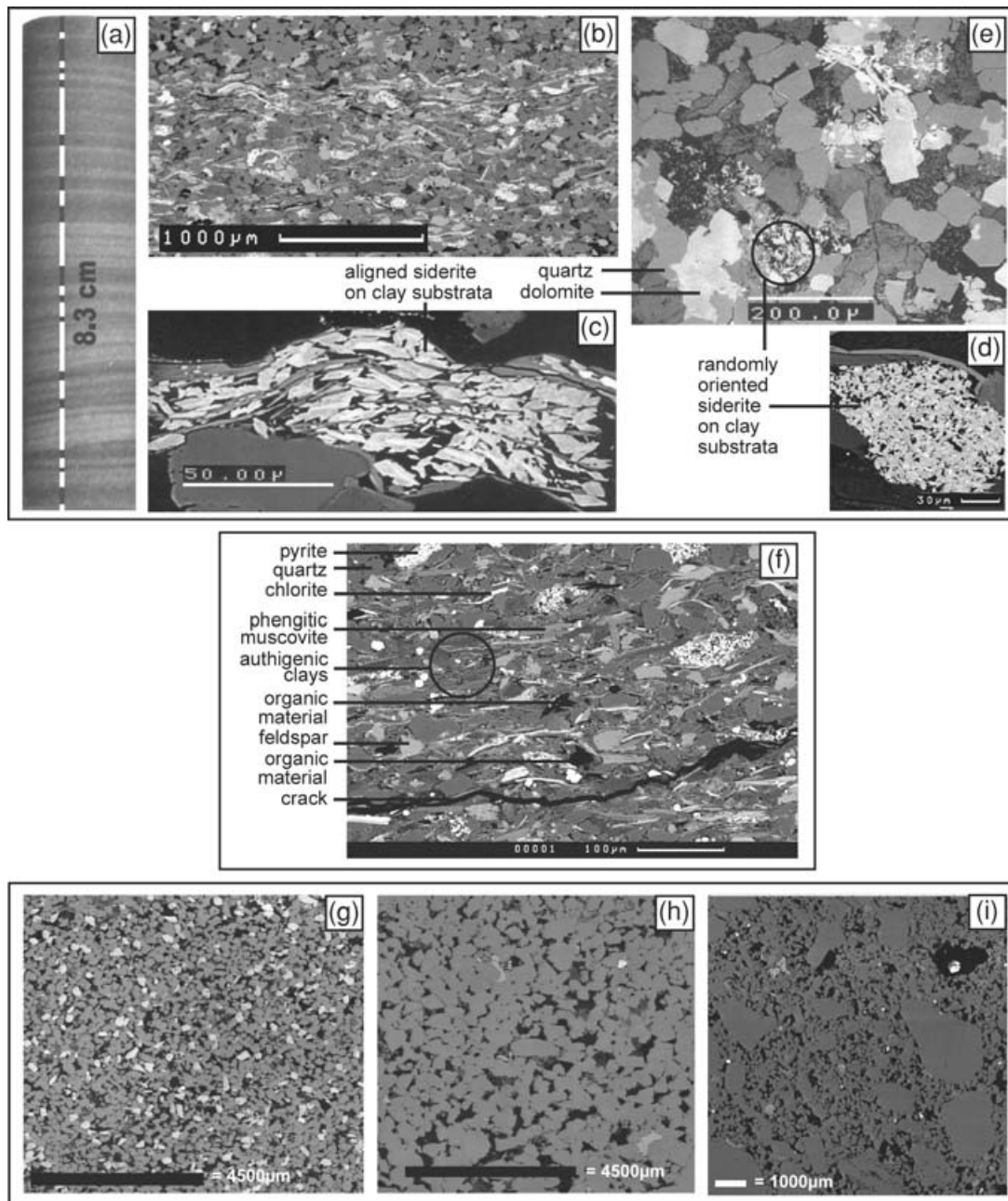
Figure 2. Microstructures and main constituent minerals of used samples. (b)–(i): BSE atomic number (*Z*) contrast images; grey-scale is mineral specific, for legend see (e) and (f). (a) SV1: borehole core from which siltstone sample SV1 was taken, showing alternating sand-rich (light grey) and mud-rich (dark grey) lithologies. The model layer-stack is indicated in black (mud rich) and white (sand rich). (b) SV1: mud-rich lithology. (c) SV1: siderite growth on aligned phyllosilicate substrata. (d) SV1: siderite growth on random phyllosilicate substrata. (e) SV1: sand-rich lithology. (f) SV2: shale. (g) SV6: sandstone. (h) SV7: sandstone. (i) SV8: sandstone.

according to their relative proportions. The LPO is similar to dolomite with a preferred orientation of *c*-axes at ∼40° to the bedding plane normal and girdles of *a*-axes and *m*-poles oblique to bedding. Manual EBSD analysis of feldspar grains (not shown) suggests that they have a random orientation.

4.1.2 SV2—shale (Fig. 4a)

The successful indexing rate of EBSD of quartz was very low (Table 1) and consequently these EBSD data were not used. However, it is likely that these equant, small grains do not exhibit a preferred orientation due to sedimentary processes and, therefore, a random ODF is assumed. The XTG LPO analyses for muscovite, biotite and illite and for chlorite and kaolinite both show a concentration of *c*-axes normal to bedding. There is little random illite or kaolinite so that there was no significant dispersion of the diffraction peaks.

4.1.3 SV6—sandstone (Fig. 4b)

The quartz LPO is near random, with the maximum m.u.d. varying between 1.18 and 1.53 (Fig. 4). However, the quartz *c*-axes tend to

(a) Quartz

(b) Dolomite

(c) Siderite
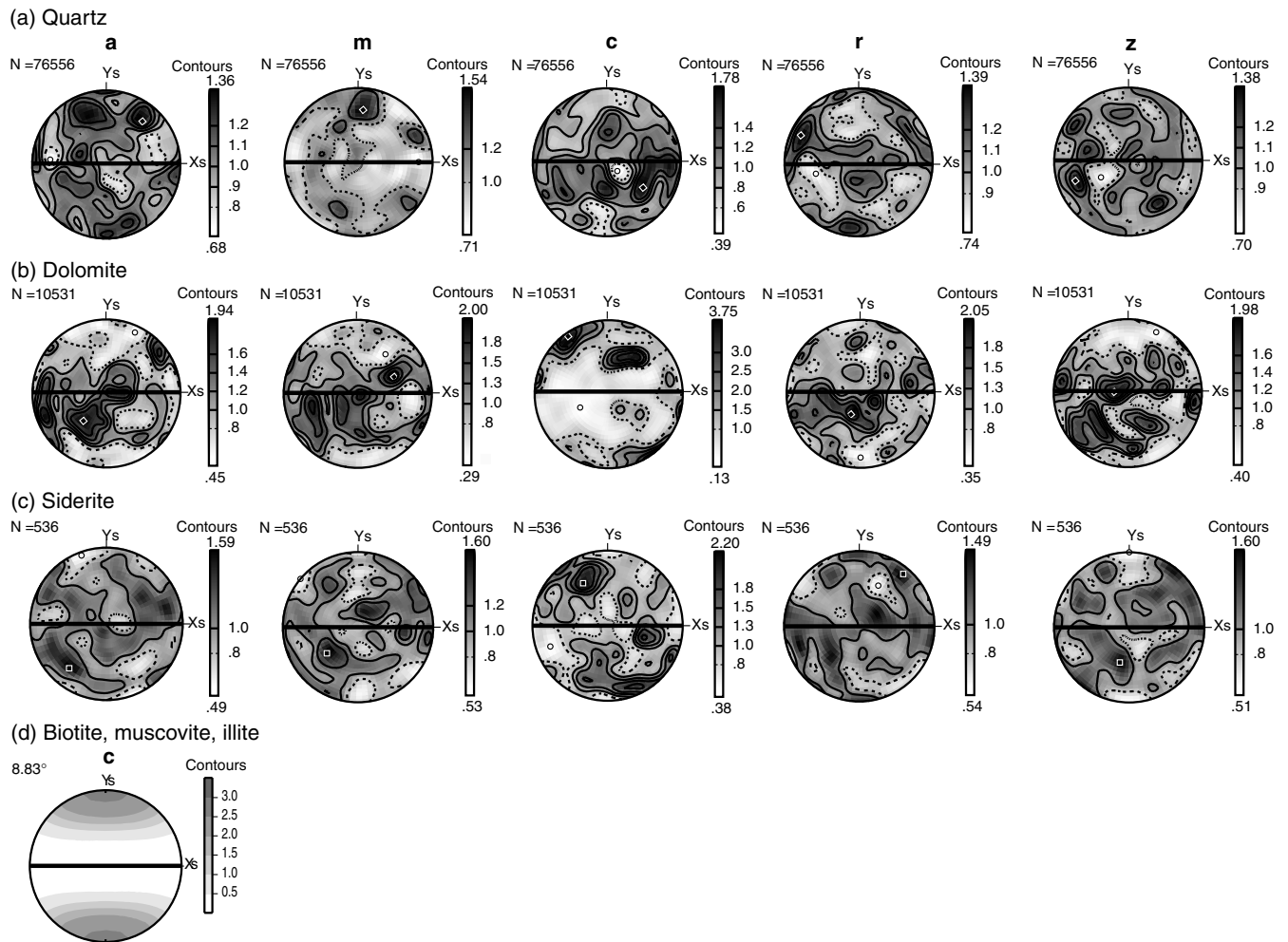

(d) Biotite, muscovite, illite

Figure 3. LPO for minerals in the siltstone sample SV1. The orientation of bedding is indicated by the thick black line. All contours are m.u.d.; maximum and minimum values are indicated by the solid black squares and open circles, respectively. (a) Quartz - EBSD derived. (b) Dolomite—EBSD derived. (c) Siderite—EBSD derived. (d) Phyllosilicates (muscovite and biotite) and clays (illite)—normalized transmission XTG derived.

lie in planes subparallel (10°–20°) to bedding, with an alignment subparallel to the X_s-axis of projection. The LPO of albite (not shown) was measured by manual EBSD analysis of 200 grains and is effectively random.

4.1.4 SV7—sandstone (Fig. 4c)

Although the LPO of quartz (maximum m.u.d. 1.45–2.56) is stronger than in samples SV1 and SV6, there is no obvious concentration of *c*-axes subparallel to bedding. Rather, several concentrations occur aligned at both small and high angles to bedding. The LPO of albite was not measured but was assumed to be random, analogous to samples SV1 and SV6.

4.1.5 SV8—sandstone (Fig. 4d)

The quartz LPO is the strongest (maximum m.u.d. 1.68–3.81) of the quartz measured in the other samples and shows a concentration of *c*-axes subparallel to bedding. The LPO of albite was not measured but was assumed to be random, again by analogy with samples SV1 and SV6.

4.2 Predicted seismic properties

4.2.1 SV1—siltstone (Fig. 5)

Layering in siltstone SV1 is well defined and forms an ideal case study to compare the anisotropy of different lithologies and to predict the effect of thin layering. Initially, therefore, the seismic properties of SV1 are predicted for the sand-rich and mud-rich lithologies separately. The data are then combined to model the long-wavelength layering-induced anisotropy using Backus-type averaging, with the mud-rich/sand-rich ratio being 37/63 according to the layer model shown on Fig. 2(a) (see also Table 3). Both the elastic constants and velocity pole figures of the mud-rich layers show that the seismic properties are close to VTI in symmetry (i.e. minima in V_P and AV_S are perpendicular to layering, whilst the maxima are layer-parallel with no preferred azimuths). The values of AV_P and AV_S are 4.5 and 3.7 per cent, respectively. The seismic properties for sand-rich layers also show a VTI-like symmetry, with minima in V_P and AV_S subparallel to the layering normal. However, in comparison with the mud-rich layers, the contour lines have less radial symmetry, whilst AV_P and AV_S are lower at 3.4 and 3.0 per cent, respectively. The seismic properties for the layer-stack have minima in V_P and AV_S normal to layering. The fastest *P*-waves have radial
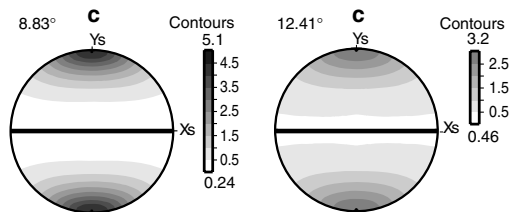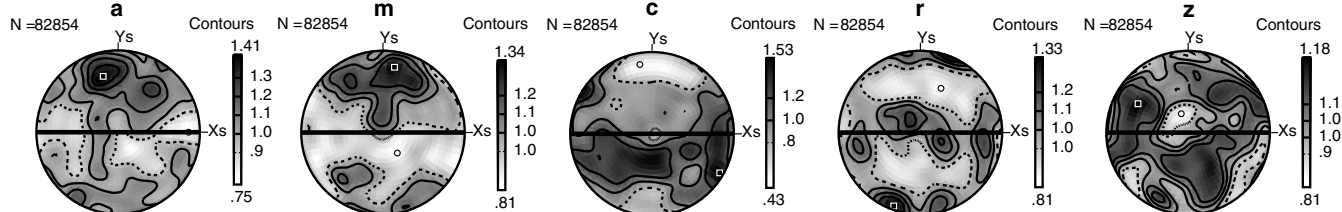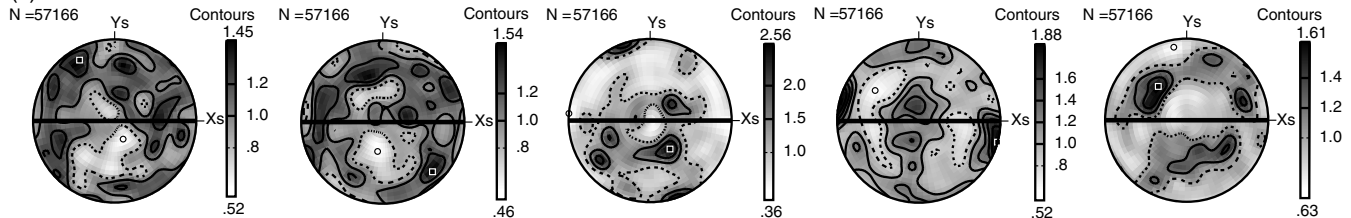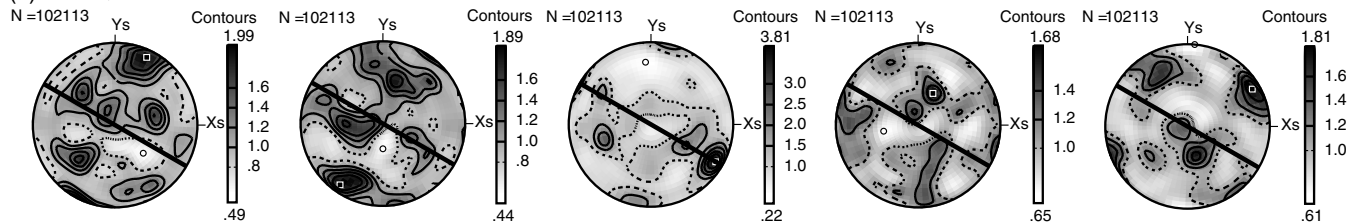
Figure 4. LPO for minerals in the shale (SV2) and sandstone (SV6, SV7, SV8) samples. The orientation of bedding is indicated by the thick black line. All contours are m.u.d.; maximum and minimum values are indicated by the solid black squares and open circles, respectively. (a) SV2: normalized transmission XTG-derived LPO for phyllosilicate and clay minerals: (left-hand panel) combined muscovite, biotite and illite; (right-hand panel) chlorite and kaolinite. (b) SV6: EBSD-derived LPO for quartz. (c) SV7: EBSD-derived LPO for quartz. (d) SV8: EBSD-derived LPO for quartz.

symmetry parallel to layering. The *S*-wave splitting is largest also parallel to layering but has less radial symmetry. Values of AV_P (3.7 per cent) and AV_S (3.1 per cent) are intermediate to those calculated for the mud-rich and sand-rich layers, although both AV_P and AV_S are somewhat closer to the latter due to the higher concentration of sand layers in the layer-stack.

4.2.2 SV2—shale (Fig. 6a)

This sample shows VTI symmetry for both *P*- and *S*-waves. The minima in both V_P and AV_S are perpendicular to bedding and their contours have radial symmetry parallel to bedding. The anisotropy is large both for *P*-waves (11.1 per cent) and *S*-wave splitting (9.8 per cent).

4.2.3 SV6—sandstone (Fig. 6b)

The symmetry of *P*-wave velocities is similar to VTI but has less radial symmetry. The minimum in V_P is at an angle of 20° to the bedding-normal. The *S*-wave splitting exhibits an irregular contour pattern and the positions of the maximum and minimum values are ill defined. The values of both AV_P and AV_S are small at 1.5 and 1.4 per cent, respectively.

4.2.4 SV7—sandstone (Fig. 6c)

This sample does not exhibit VTI symmetry and its contour lines are irregular. The maximum in AV_S (3.1 per cent) is larger than AV_P (2.6 per cent).

4.2.5 SV8—sandstone (Fig. 6d)

The minimum in V_P is perpendicular to bedding and the maximum is bedding-parallel. However, the contour lines do not show VTI symmetry. The *S*-wave splitting exhibits also an irregular contour pattern apparently unrelated to bedding, with the positions of the maximum and minimum values ill defined. The maximum *S*-wave splitting (2.5 per cent) is larger than the *P*-wave anisotropy (2.1 per cent).

Cij coefficients

Seismic wave phase velocities

(a) SV1 - mud-rich layer

```
1.1606    0.3104    0.3107   -0.0002    0.0006    0.0006
0.3105    1.1638    0.3132    0.0014   -0.0009    0.0017
0.3115    0.3133    1.0647   -0.0032   -0.0019   -0.0013
-0.0010  -0.0005   -0.0021    0.3973   -0.0003   -0.0012
-0.0029  -0.0007    0.0022   -0.0004    0.3957   -0.0015
0.0008    0.0014   -0.0014    0.0004   -0.0006    0.4221
```

Vp

Contours (km s^{-1})
6.15
6.20
6.25
6.30
6.35
6.43

Anisotropy = 4.5%

AVs

Contours (%)
0.00
0.50
1.00
1.50
2.00
2.50
3.00
3.72

Vs1 Polarization planes

(b) SV1 - sand-rich layer

```
1.1585    0.2978    0.2941   -0.0005    0.0026   -0.0074
0.2963    1.1676    0.3000   -0.0094   -0.0005    0.0027
0.2959    0.2985    1.0995   -0.0023    0.0070   -0.0014
-0.0011  -0.0090   -0.0024    0.4214   -0.0021    0.0002
0.0050   -0.0005    0.0050   -0.0018    0.4165   -0.0015
-0.0071    0.0028   -0.0018   -0.0003   -0.0011    0.4334
```

Contours (km s^{-1})
6.32
6.36
6.38
6.40
6.42
6.44
6.46
6.48
6.50
6.52
6.54

Anisotropy = 3.4%

Contours (%)
0.08
1.00
1.50
2.00
2.50
3.03

(c) SV1 - layerstack

```
1.1592    0.3014    0.3016   -0.0011    0.0021   -0.0043
0.3023    1.1661    0.3039   -0.0058   -0.0006    0.0023
0.3002    0.3048    1.0867   -0.0023    0.0039   -0.0017
-0.0004  -0.0054   -0.0026    0.4124   -0.0013    0.0000
0.0019   -0.0006    0.0036   -0.0014    0.4088   -0.0009
-0.0045    0.0023   -0.0014   -0.0003   -0.0015    0.4293
```

Contours (km s^{-1})
6.25
6.30
6.40
6.49

Anisotropy = 3.7%
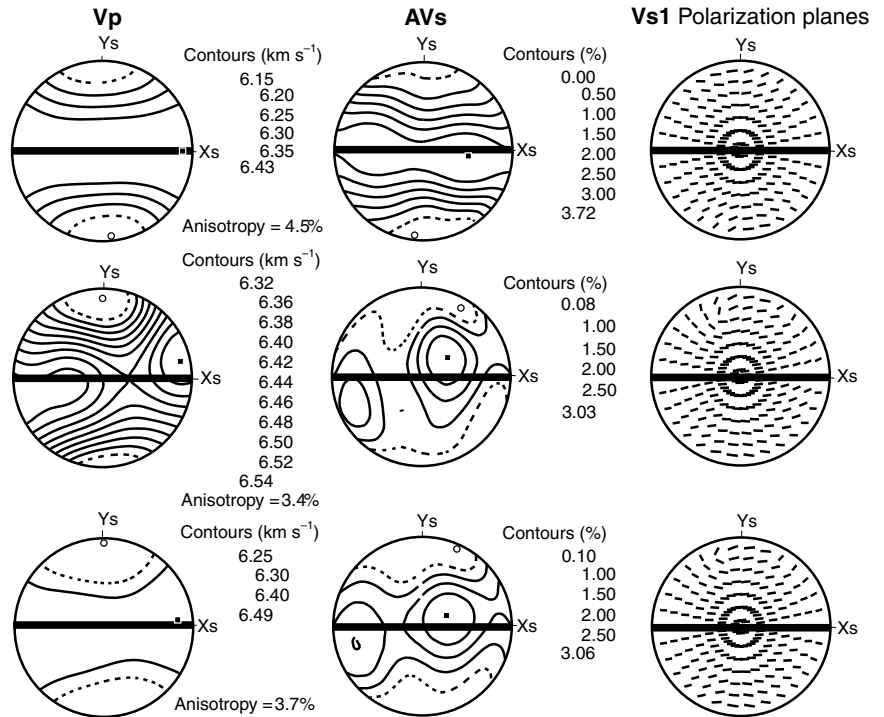
Contours (%)
0.10
1.00
1.50
2.00
2.50
3.06

Figure 5. Elasticity C_{ij} coefficients (10^{-2} GPa) and seismic predictions (*P*-wave phase velocity, km s^{-1}, *S*-wave splitting, per cent, and polarization planes) for siltstone sample SV1. Maximum and minimum values are indicated by the solid black squares and open circles, respectively. (a) Mud-rich lithology. (b) Sand-rich lithology. (c) Layer-stack: combined mud-rich and sand-rich layer lithologies.

5 DISCUSSION

No specific geological context is available for the samples analysed in this study because the samples were collected from different boreholes in different hydrocarbon reservoirs. However, we can more generally discuss the geological context and significance of the results. First, potential geological explanations are suggested for the LPO observed in the samples, using also data available in the literature. Secondly, the influence of the sample lithology on the LPO-related anisotropy is considered. Thirdly, the influence of the individual minerals on seismic anisotropy is investigated.

5.1 Sedimentary LPO

Fabrics in sedimentary rocks are in general related to deposition and compaction processes and are therefore largely dependent on depositional environment, composition and post-depositional burial effects such as stress and temperature. Although relatively little attention has been given to the occurrence of LPO in sedimentary rocks, it has long been recognized. A brief summary is given of the known occurrences of LPO in sedimentary rocks and of the significance in the context of the observed LPO in this study for the individual mineral constituents.

5.1.1 Quartz

Elongate detrital quartz grains can have a shape preferred orientation (SPO) related to water flow conditions (e.g. Hiscott & Midlleton 1980; Baas 2000). Quartz grains are imbricated at low angles to bedding when they are deposited under a flow current. Furthermore, the

long axes are parallel to the flow direction when small grains have settled from suspension, while they are perpendicular to the flow direction when relatively large grains are subject to rolling transport over the bed surface (Baas 2000). Such SPO behaviour appears to hold for a wide range of grain sizes, including down to 0.1 mm^2 (Baas, private communication, 2003), which is significant for the samples considered in this study. Finally, it has been observed, and is often assumed, that the long axis of elongate quartz grains in sedimentary rocks is parallel to the *c*-axis, although this may not always be the case (e.g. Pettijohn 1975; Prior & Sims 1986). These observations suggest that the quartz LPO observed in the samples considered here could be related to SPO due to specific water flow conditions. Indeed, the *c*-axes concentration around a plane at 20° to the bedding in samples SV1 and SV6 (Figs 3a and 4b) may be an indication of imbricated quartz grains deposited under current flow. The spread of the *c*-axes might be due to slight variations in the current flow direction. In samples SV7 and SV8, the tendency for bedding-parallel fabrics (Figs 6c and d), might be due to settling of grains under specific water-flow conditions. However, the lineations at different angles to bedding are related to large individual grains rather than to specific sedimentary conditions. This is due to the fact that large grains constitute a high number of measurement points on the EBSD grid with the same crystal orientation, and thus dominate the LPO. Unfortunately, the EBSD map size that is used, is the maximum size possible in our EBSD set up. Therefore, more samples from the same rock type should be analysed and their LPO combined to sample the large grains in a statistically representative way. The significance of authigenic quartz growth on LPO development has not been investigated in this study. However, as authigenic quartz tends to grow in crystallographic continuity with

Cij coefficients

Seismic wave phase velocities

Vp   **AVs**   **Vs1** Polarization planes

(a) SV2

1.1198	0.3342	0.3225	-0.0010	-0.0007	-0.0005
0.3342	1.1309	0,3188	0,0032	0.0001	-0.0005
0.3225	0.3188	0.9055	0.0007	-0.0001	0.0003
-0.0010	0.0032	0.0007	0.3288	0.3272	0.0012
-0.0007	0.0001	-0.0001	-0.0001	0.3272	0.0012
-0.0005	-0.0005	0.0003	-0.0004	0.0012	0.3979

Contours (km s^{-1}): 5.85, 6.00, 6.10, 6.15, 6.20, 6.30, 6.40, 6.53
Anisotropy = 11.1%

Contours (%): 0.06, 2.00, 3.00, 4.00, 5.00, 6.00, 7.00, 8.00, 9.80

(b) SV6

0.9540	0.1189	0.1195	-0.0016	-0.0034	0.0008
0.1189	0.9459	0.1235	-0.0015	0.0008	-0.0012
0.1195	0.1235	0.9355	0.0094	0.0017	0.0006
-0.0016	-0.0015	0.0094	0.4114	0.0007	0.0002
-0.0034	0.0008	0.0017	0.0007	0.4099	0.0026
0.0008	-0.0012	0.0006	0.0002	0.0026	0.4158

Contours (km s^{-1}): 5.95, 5.97, 5.98, 5.99, 6.00, 6.01, 6.02, 6.03, 6.04
Anisotropy = 1.5%

Contours (%): 0.00, 0.20, 0.40, 0.60, 0.80, 1.00, 1.20, 1.44

(c) SV7

0.9673	0.1066	0.1065	-0.0017	-0.0025	0.0050
0.1066	0.9772	0.1131	-0.0036	-0.0026	0.0013
0.1065	0.1131	0.9685	0.0140	0.0066	-0.0046
-0.0017	-0.0036	0.0140	0.4368	-0.0035	-0.0017
-0.0025	-0.0026	0.0066	-0.0035	0.4194	0.0039
0.0050	0.0013	-0.0046	-0.0017	0.0039	0.4252

Contours (km s^{-1}): 5.96, 5.98, 6.00, 6.02, 6.04, 6.06, 6.08, 6.11
Anisotropy = 2.6%

Contours (%): 0.02, 1.00, 1.50, 2.00, 2.50, 3.11

(d) SV8

0.9709	0.1259	0.1265	-0.0058	-0.0024	-0.0078
0.1259	0.9553	0.1357	0.0080	0.0026	0.0038
0.1265	0.1357	0.9498	0.0057	-0.0057	0.0023
-0.0058	0.0080	0.0057	0.4280	0.0013	-0.0009
-0.0024	0.0026	-0.0057	0.0013	0.4230	-0.0006
-0.0078	0.0038	0.0023	-0.0009	-0.0006	0.4258

Contours (km s^{-1}): 5.97, 6.00, 6.02, 6.04, 6.06, 6.10
Anisotropy = 2.1%

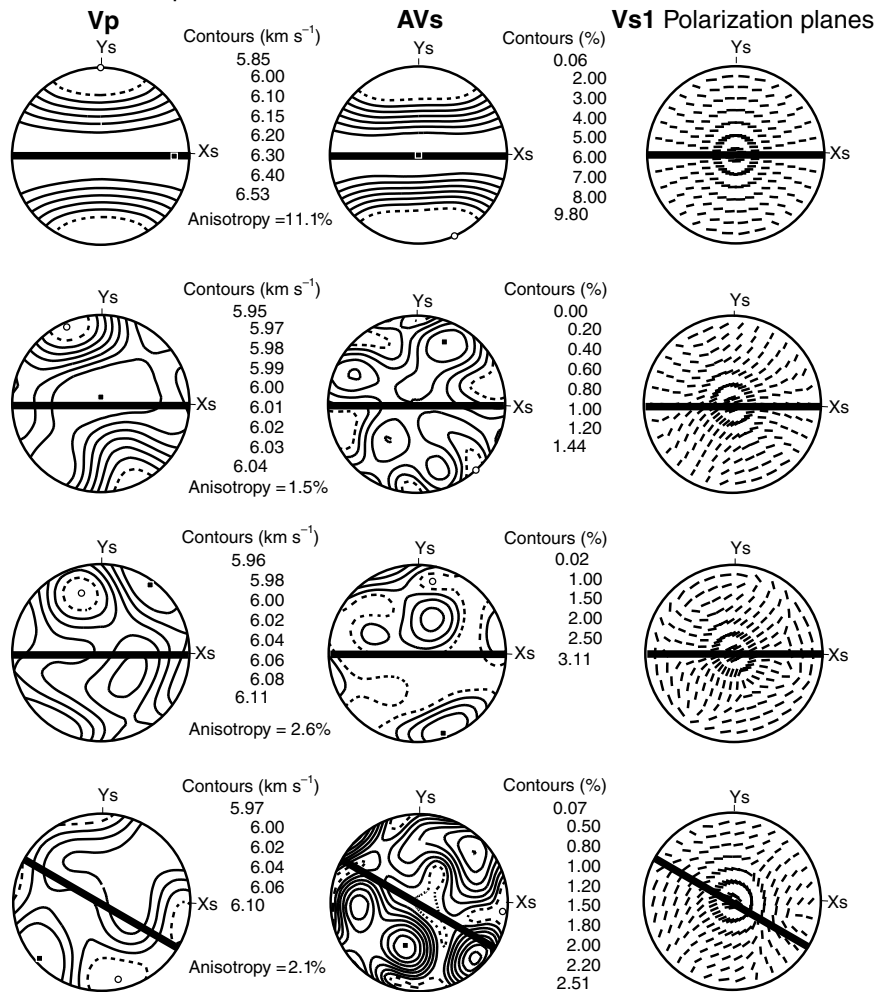Contours (%): 0.07, 0.50, 0.80, 1.00, 1.20, 1.50, 1.80, 2.00, 2.20, 2.51

Figure 6. Elasticity C_{ij} coefficients (10^{-2} GPa) and seismic predictions (*P*-wave phase velocity, km s^{-1}, *S*-wave splitting, per cent, and polarization planes) for the siltstone and sandstone samples. Maximum and minimum values are indicated by the solid black squares and open circles, respectively. (a) SV2. (b) SV6. (c) SV7. (d) SV8.

detrital grains (Deer *et al.* 1992), it is likely that authigenic quartz growth will enhance any initial LPO due to the detrital quartz grains and primary sedimentary processes.

5.1.2 Carbonate minerals

Diagenetic carbonate minerals, such as calcite, dolomite and siderite, often have a specific *c*-axis preferred orientation in sedimentary rocks (e.g. Attewell *et al.* 1969; Bellamy 1977; Hounslow 2001). The two main trends observed are bedding-parallel with no preferred direction and bedding-normal with a subsidiary girdle grouping of *c*-axes at ~44° to the normal. These carbonate LPO seem to be dictated by the preferred orientation of the nucleation substrate (Archibald *et al.* 1996; Hounslow 2001). Both dolomite and siderite in sample SV1 have a concentration of *c*-axes from 45° to 90° to bedding. It is clear from photomicrographs that this fabric is related to growth on mica substrata. This is particularly apparent for siderite, where one side of the siderite rhombohedra is parallel to the elongate side of the phyllosilicates (Fig. 2c). As the latter are subparallel to the bedding, the siderite also has a preferred orientation related to the bedding. Furthermore, where siderite has grown

in relation to randomly oriented clay, the siderite is likewise random (Fig. 2d).

5.1.3 Feldspars

There is no published literature on the LPO of detrital feldspar grains. The manually measured LPO in SV6 seems near-random. Authigenic feldspar overgrowths probably enhance the random LPO fraction as they tend to be growth rims with many randomly oriented subgrains (e.g. Parnell 1992; Worden & Rushton 1992).

5.1.4 Phyllosilicates and clays

The LPO of detrital phyllosilicates is potentially very strong in sedimentary rocks, with a concentration of *c*-axes normal to bedding and *a*- and *b*-axes lying randomly within the bedding. This is due to deposition in stagnant water and mechanical compaction of the elongate platelets (e.g. Kaarsberg 1959; Bjorlykke 1998; Hornby 1998). This type of LPO is observed for phyllosilicate *c*-axes in samples SV1, SV2, and SV5. The random orientation of *a*- and *b*-axes within the bedding was confirmed with the EBSD analysis of sample SV1 (Valcke 2003). Authigenic clays are known to precipitate on and/or

replace detrital phyllosilicates during diagenesis (Bjorlykke 1998). Thus, many authigenic clays are likely to have similar LPO characteristics as detrital phyllosilicates. However, authigenic clays that are pore filling typically have a random orientation. The authigenic clays in the samples SV1 and SV2 show a concentration of *c*-axes (= short shape axis) normal to bedding and *a*- and *b*-axes lying randomly within the bedding, consistent with the behaviour of the associated detrital phyllosilicates.

5.2 Influence of lithology on LPO-related seismic anisotropy

The predicted seismic anisotropy for all samples considered lies between 1.5 and 11.1 per cent for *P*-wave and between 1.4 and 9.8 per cent for maximum *S*-wave splitting (Table 3). The degree of anisotropy is related to lithology and decreases from the shale to siltstone to sandstone. The *P*-wave anisotropy is typically similar to, or a few per cent larger than, the maximum *S*-wave splitting for most of the samples. However, in sandstone samples SV7 and SV8, the *S*-wave splitting is larger than the *P*-wave anisotropy. Lithological characteristics that influence the amount of LPO-dependent seismic anisotropy can be deduced therefore from the following results.

(1) The main factor is the mineralogy of the rock. Phyllosilicate-rich samples have anisotropy values that are much higher (SV1, SV2) than those in quartz-rich samples (SV6, SV7, SV8). The siltstone having intermediate proportions of phyllosilicates and quartz, has an intermediate degree of anisotropy. The mineralogy also influences the symmetry of the anisotropy. The *P* waves of phyllosilicate-rich samples approach VTI symmetry, with the symmetry axes perpendicular to bedding, while in the quartz-rich samples, the symmetry is less VTI to non-VTI (no radial symmetry). The *S*-waves only show VTI symmetry in the samples with a large amount of phyllosilicates (mud-rich layers of SV1 and SV2). In the other samples the symmetry is non-VTI.

(2) A second important factor is the burial depth of the samples, a factor which also has been observed in ultrasonic studies (Jones & Wang 1981; Tosaya & Nur 1982; Hornby 1998). Increasing burial is likely to result in increased mechanical compaction and mesodiagenetic alteration. Mechanical compaction may enhance any primary LPO directly (especially that of phyllosilicates), whilst mesodiagenetic alteration improves, for example, the crystallinity of authigenic clays. An increase in strength of LPO will affect seismic anisotropy. The deeply buried, coarser and more-cemented sandstones, SV7 and SV8, show slightly larger anisotropy than the shallowly buried, finer-grained and less-cemented sandstone, SV6. However, this trend might be explained by the LPO related to large grains and sedimentary flow conditions at the time of deposition (see 5.1). More analyses of sandstones and of shales, with similar original grain size distribution and composition, but from different depths, are required to investigate the influence of burial depth.

(3) Thin periodic layering is another lithology-related factor that can influence the amount of seismic anisotropy. However, the layering in the siltstone sample (SV1) does not cause additional anisotropy for long-wavelength propagation, probably due to the small differences in density and in elasticity between the two layer types.

5.3 Influence of individual minerals on LPO-related seismic anisotropy

It was shown previously that different mineral phases not only have different single-crystal seismic properties, but also develop different LPO in sedimentary rocks. Consequently, each mineral has its own specific influence on seismic anisotropy according to its modal content. This section considers the impact of the constituent minerals on sample seismic anisotropy.

5.3.1 Quartz

In general, a significant amount of quartz with a near-random LPO appears to decrease the seismic anisotropy (e.g. Fig. 5, SV1 sand-rich type versus SV1 mud-rich type). However, any quartz LPO that does exist may act to increase sample anisotropy. For example, due to its low mica and high quartz contents, the seismic characteristics of sample SV6 are due mainly to the quartz LPO, which has *c*-axes subparallel to bedding and *a*-axes, *m*- and *r*-poles at high angles to bedding. Single-crystal quartz exhibits low *P*-wave velocities close to the basal plane (*a*-, *m*- and *r*-poles) and high velocities subparallel to the *c*-axis and *z*-pole (e.g. Lloyd 2000, fig. 10). Consequently, the combination of the quartz LPO and single-crystal elasticity causes the seismic properties of sample SV6 to approach VTI with the minimum velocity axis subnormal to bedding and high velocities subparallel to bedding (Fig. 6b). Furthermore, this potential VTI-causing effect of quartz LPO enhances the VTI due to muscovite and siderite in the mud-rich layers and due to dolomite in the sand-rich layers of sample SV1 (see below).

Thus, the LPO and symmetry of seismic anisotropy of *P*-waves possibly may be used in quartz-rich rock types to infer bedding and/or also flow direction, if the latter causes a well-developed lineation. In contrast to *P*-wave velocities, *S*-wave splitting in quartz single crystals has a complex distribution, which is probably why the *S*-waves show irregular distributions for the sandstone samples SV6, SV7 and SV8.

5.3.2 Carbonate minerals

Dolomite and siderite single crystals have minimum *P*-wave velocity parallel to the *c*-axis and maximum velocity parallel to the basal plane with no preferred azimuthal trend (Bass 1995; Chen *et al.* 2001). Consequently, a sedimentary carbonate LPO with *c*-axes subperpendicular to layering (SV1) causes VTI, with the symmetry axis subnormal to layering. For example, the VTI-causing effect of the dolomite LPO can be seen in the *P*-waves of the sand-rich layers of SV1, although the overall VTI symmetry is a combination of dolomite, quartz and mica effects. Also, the siderite LPO in the mud-rich lithology in SV1 contributes to the overall VTI, which is mainly due to the phyllosilicate content (see below). In contrast to *P*-wave velocities, *S*-wave splitting in carbonate single crystals is complex and there is unlikely to be a simple relationship between carbonate LPO and sample *S*-wave properties.

5.3.3 Phyllosilicate and clay minerals

Phyllosilicate single crystals exhibit a strong anisotropy with minimum *P*- and *S*-wave velocities parallel to the *c*-axis and maxima parallel to the basal plane with no preferential azimuthal trend (Vaughan & Guggenheim 1986; Katahara 1996). Consequently, typical sedimentary phyllosilicate LPO with *c*-axes perpendicular to layering and *a*- and *b*-axes with no preferential alignment (e.g. SV1, SV2) cause VTI symmetry for both *P*- and *S*-waves, with a symmetry axis normal to bedding. The influence of phyllosilicates dominates the seismic wave characteristics of SV2 and the mud-rich layers of SV1, due to their strong single-crystal anisotropy, strong LPO (Figs 3 and 4) and also their relatively high modal proportions (Table 3). Both SV1 (mud rich) and SV2 have symmetry axes for *P*- and *S*-waves

normal to layering, rather than subnormal if quartz and/or carbonate minerals were dominating the seismic properties. However, the presence of randomly oriented pore-filling authigenic clays may reduce the VTI-causing effect of aligned phyllosilicates.

5.3.4 Feldspar minerals

Feldspars are typically randomly oriented and therefore, regardless of their single-crystal anisotropy, will not strengthen the overall seismic anisotropy in any sample. However, in the samples considered in this study, feldspar modal proportions were relatively minor and so did not significantly influence either the magnitude or symmetry of the sample seismic anisotropy.

5.3.5 Other minerals

Most other minerals (e.g. pyrite) recognized in the samples are present in only accessory proportions. In general, they are randomly oriented and regardless of their single-crystal anisotropy have negligible impact on either the magnitude or symmetry of the aggregate seismic anisotropy.

5.4 Comparison with ultrasonic measurements

It is not straightforward to constrain exactly how much of the total anisotropy determined from published ultrasonic measurements is due to LPO. Many factors affect the total seismic anisotropy (Section 1). Here, we have quantified the contribution from LPO in a range of samples and have shown that LPO is responsible for a significant proportion of the anisotropy in sedimentary rocks. Our results for sandstone and siltstone compare well with those derived from ultrasonic measurements (Wang 2002). However, anisotropy of shales shows a much wider variability (Jones & Wang 1981; Tosaya 1982; Jakobsen & Johansen 2000; Vernik & Nur 1992; Hornby 1998; Wang 2002). More direct comparisons with ultrasonic measurements from the literature require a better quantification of other factors that will affect anisotropy, such as pore alignment. Ideally, direct comparisons between LPO-related anisotropy and total anisotropy measured using ultrasonics should be made on the same samples.

6 CONCLUSIONS

This study has investigated the LPO of minerals in five sedimentary rock samples: shale (SV2), siltstone (SV1) and sandstones (SV6, SV7, SV8), using SEM EBSD and XTG. The measured LPO were used to predict the seismic anisotropy in each sample. The contribution of different minerals to the sedimentary fabric and seismic anisotropy has been assessed. The conclusions of this investigation can be summarized as follows.

(1)   A combination of EBSD and XTG can be used to determine the LPO of most minerals in sedimentary rocks. Automated EBSD measurements are reliable for quartz and carbonates, but may be inaccurate for low-symmetry minerals, such as feldspars, phyllosilicates and authigenic clays, due to their crystallographic complexity and the low quality of their EBSD patterns. Manual EBSD measurements are often suitable for these minerals. Alternatively, automated XTG can be used to measure the LPO of phyllosilicate minerals. However, this approach provides only the *c*-axis orientations and assumes radial symmetry in the LPO.

(2)   The strongest LPO are observed for phyllosilicates and occur, in descending order, in the shale, siltstone and sandstones. The

phyllosilicates are oriented with their basal plane subparallel to bedding but with no preferred direction in the bedding plane, which is a typical sedimentary fabric due to depositional and compaction processes. In contrast, authigenic pore-filling clays tend to be randomly oriented in the siltstone and sandstones. Relatively strong LPO were measured for diagenetic dolomite and siderite, with *c*-axis concentrations at 45°–90° to bedding probably due to controlled growth on aligned phyllosilicate substrata. Quartz LPO are typically near random, although in SV1 and SV6 the *c*-axes do show a weak concentration in a girdle at 10°–20° from the bedding, possibly due to imbrication of elongate quartz grains deposited via current flow. The LPO of feldspars proved difficult to measure via automated EBSD, but manual EBSD analyses suggest that their LPO are random.

(3)   The LPO for the individual minerals in each sample were combined based on their modal proportions with the respective single-crystal elastic properties to predict the seismic anisotropy of the sedimentary rocks via a VRH averaging scheme. The predicted *P*-wave anisotropy lies between 1.5 and 11.1 per cent, whilst the predicted maximum *S*-wave splitting lies between 1.4 and 9.8 per cent, with lowest values in the sandstones, intermediate values in the siltstone and highest values in the shale.

(4)   The main lithological characteristic in the samples that has a positive influence on LPO-dependent seismic anisotropy is the phyllosilicate content. In cases where the seismic anisotropy is significant (i.e. >2 per cent), symmetry is VTI, with symmetry axis normal to bedding, mainly due to the phyllosilicate influence. However, the LPO of dolomite and siderite also tend to add to the VTI symmetry. In quartz-rich, weakly anisotropic samples, the symmetry is not VTI, although it may approach VTI, with symmetry axis at a small angle to the bedding plane normal, when quartz shows a sedimentary LPO. Thin periodic layering (e.g. in the siltstone sample SV2) does not seem to have a significant effect on long-wavelength anisotropy, provided density and anisotropy differences between the combined layer lithologies are low.

The results reported in this study support suggestions made in previous studies that phyllosilicate LPO is an important cause of seismic anisotropy in shales. In addition, they also show that a few per cent anisotropy can be caused by the LPO of quartz, dolomite and siderite in siltstones and sandstones.

REFERENCES

Alkhalifah, T. & Rampton, D., 2001. Seismic anisotropy in Trinidad: a new tool for lithology prediction, The Leading Edge, April 2001, 420–424.

Archibald, D.D., Qadri, S.B. & Gaber, N.P., 1996. Modified calcite deposition due to ultrathin organic films on silicon substrates, *Langmuir,* **12,** 538–546.

Attewell, P.B., Hirst, D.M. & Taylor, R.K., 1969. Diagenetic recrystallisation and orientation of two carbonate species, *Sedimentology,* **14,** 237–247.

Baas, J.H., 2000. Experimental research on hydraulics and depositional mechanisms of high-density turbidity currents, Final Report for TMR Marie Curie Fellowship Programme, pp. 187, European Union, Brussels.

Babuska, V. & Cara, M., 1991. *Seismic anisotropy in the Earth, Modern Approaches in Geophysics,* Vol. 10, pp. 217, Kluwer Academic Publishers, Dordrecht.

Backus, G.E., 1962. Long-wave elastic anisotropy produced by horizontal layering, *J. geophys. Res.,* **67,** 4427–4440.

Banik, N.C., 1984. Velocity anisotropy of shales and depth estimation in the North Sea basin, *Geophysics,* **49,** 1411–1419.

Bass, J.D., 1995. Elasticity of minerals, glasses and melts, in *Mineral Physics and Crystallography: A Handbook of Physical Constants*, pp. 45–63, ed. Ahrens, T.J., American Geophysical Union, Washington.

Bellamy, J.R.W., 1977. Surface expansion megapolygons in Upper Jurassic dolostone (Kimmeridge, UK), *Journal of Sedimentary Petrology,* **47,** 973–978.

Bjorlykke, K., 1998. Clay mineral diagenesis in sedimentary basins—a key to prediction of rock properties. Examples from the North Sea Basin, *Clay Minerals,* **33,** 15–34.

Blackman, D.K. & Kendall, J.M., 2002. Seismic anisotropy in the Upper Mantle: 2. Predictions for current plate boundary flow models, *Geochemistry, Geophysics, Geosystems—G*^{3}*,* **3,** 18.

Blackman, D.K., Wenk, H.R. & Kendall, J.M., 1996. Seismic anisotropy of the upper mantle: 1, factors that affect mineral texture and effective elastic properties, *Geophys. J. Int.,* **127,** 415–426.

Carlson, C.H., Schaftenaar, C.H. & Moore, R.P., 1984. Causes of compressional-wave anisotropy in carbonate bearing, deep-sea sediments, *Geophysics,* **49,** 525–532.

Casey, M., 1981. Numerical analysis of X-ray texture data: an implementation in Fortran allowing triclinic or axial specimen symmetries and most crystal symmetries, *Tectonophysics,* **40,** 257–285.

Chen, C-C., Lin, C-C., Liu, L-G., Sinogeikin, S.V. & Bass, J.D., 2001. Elasticity of single-crystal calcite and rhodochrosite by Brillouin spectroscopy, *American Mineralogist,* **86,** 1525–1529.

Cullity, B.D., 1978. *Elements of X-ray Diffraction*, 2nd edn, pp. 555, Addison-Wesley, London.

Deer, W.A., Howie, R.A. & Zussman, J., 1992. *An Introduction to the Rock Forming Minerals*, 2nd edn, pp. 696, Longman Scientific and Technical, Essex.

Dewhurst, D.N., Siggins, A.F. & Raven, M.D., 2002. Influence of Pore Pressure, Composition and Microstructure on the Acoustic properties of Shales, Proceedings of the SPE/ISRM Rock Mechanics Conference 20–23 October 2002, Texas, SPE/ISRM, 78197.

Herwanger, J.V., Worthington, M.H., Lubbe, R., Binley, A. & Khazanehdari, J., 2004. A comparison of crosshole electrical and seismic data in fractured rock, *Geophys. Prospect.,* **52,** 109–121.

Hess, H.H., 1964. Seismic anisotropy of the uppermost mantle under oceans, *Nature,* **203,** 629–631.

Hill, R., 1952. The elastic behaviour of a crystalline aggregate, *Proceedings of the Physical Society, London, A,* **65,** 351–354.

Hillier, S., 1999. Use of an air brush to spray dry samples for X-ray powder diffraction, *Clay Minerals,* **34,** 127–135.

Hillier, S., 2000. Accurate quantitative analysis of clay and other minerals in sandstones by XRD; comparison of a Rietveld and a reference intensity ratio (RIR) method and the importance of sample preparation, *Clay Minerals,* **25,** 291–302.

Hiscott, R.N. & Midlleton, G.V., 1980. Fabric of coarse deep-water sandstones, Tourelle Formation, Canada, *Journal of Sedimentary Petrology,* **50,** 703–721.

Hornby, B.E., 1998. Experimental laboratory determination of the dynamic elastic properties of wet, drained shales, *J. geophys. Res.,* **103,** 29 945–29 964.

Hornby, B.E., Schwartz, L.M. & Hudson, J.A., 1994. Anisotropic effective medium modeling of the elastic properties of shales, *Geophysics,* **59,** 1570–1582.

Hounslow, M.W., 2001. The crystallographic fabric and texture of siderite in concretions: implications for siderite nucleation and growth processes, *Sedimentology,* **48,** 533–557.

Hrouda, F., Pros, Z. & Wohlgemuth, J., 1993. Development of magnetic and elastic anisotropies in slates during progressive deformation, *Phys. Earth planet. Inter.,* **77,** 251–265.

Humpreys, F.J., 2001. Review: Grain and subgrain characterization by electron backscattered diffraction, *J. Mater. Sci.,* **36,** 3833–3854.

Jakobsen, M. & Johansen, T.A., 2000. Anisotropic approximations for mudrocks: A seismic laboratory study, *Geophysics,* **65,** 1711–1725.

Johnston, J.E. & Christensen, N.I., 1995. Seismic anisotropy of shales, *J. geophys. Res.,* **100,** 5991–6003.

Jones, L.E.A. & Wang, H.F., 1981. Ultrasonic velocities in Cretaceous shales from the Willington basin, *Geophysics,* **46,** 288–297.

Kaarsberg, E.A., 1959. Introductory studies of natural and artificial argillaceous aggregates by sound-propagation and X-ray diffraction methods, *J. Geol.,* **67,** 447–472.

Katahara, K.W., 1996. Clay mineral elastic properties, Society of Exploration Geophysicists, *Annual Meeting Expanded Technical Program Abstracts with Biographies,* **66,** 1691–1694.

Kern, H., 1993. *P*-wave and *S*-wave anisotropy and shear-wave splitting at pressure and temperature in possible mantle rocks and their relation to rock fabric, *Phys. Earth planet. Inter.,* **78,** 245–256.

Kern, H. & Wenk, H-R., 1985. Anisotropy in rocks and the geological significance, in *Preferred orientation in deformed metals and rocks: an introduction to modern texture analysis*, pp. 537–555, ed. Wenk, H-R., Academic Press, Orlando.

Landolt-Bornstein, 1984. Numerical data and functional relationships in Science and Technology. Group III, Crystal and solid state physics; Elastic, piezoelectric and related constants of crystals, Vol. 18, pp. 559, Springer-Verlag, Berlin.

Lee, J.M. & Alexander, S.S., 1995. Seismic anisotropy caused by rock fabric, *Geophys. J. Int.,* **122,** 705–718.

Lloyd, G.E., 2000. Grain boundary contact effects during faulting of quartzite: an SEM/EBSD analysis. *J. Struct. Geol.,* **22,** 1675–1693.

Lloyd, G.E. & Kendall, J-M., 2005. Petrofabric and seismic property evolution in a mylonitic quartz simple shear zone, in *Petrophysical Properties of Crystalline Rocks; Special Publications*, Vol. 240, pp. 75–94, ed. Harvey, P.K., Geological Society, London.

MacDonal, F.J., Angona, F.A., Mills, R.L., Sengbush, R.L., Van Nostrand, R.G. & White, J.E., 1958. Attenuation of shear and compressional waves in Pierre shale, *Geophysics,* **23,** 554–563.

Mainprice, D., 1990. A Fortran program to calculate seismic anisotropy from the lattice preferred orientation of minerals, *Computers and Geosciences,* **16,** 385–393.

Mainprice, D., Barruol, G. & Ben Ismail, W., 2000. The seismic anisotropy of the Earth's mantle; from single crystal to polycrystal, in *Earth's deep interior; mineral physics and tomography from the atomic to the global scale; Geophysical Monograph*, Vol. 117, pp. 237–264, eds Karato, S-I., Forte, A.M., Lieberman, R.C., Masters, G. & Stixrude, L., American Geophysical Union, Washington.

Mainprice, D. & Nicolas, A., 1989. Development of shape and lattice preferred orientation: application to the seismic anisotropy of the lower crust, *J. Struct. Geol.,* **11,** 175–189.

Mainprice, D., Popp, T., Guegen, Y., Huenges, E., Rutter, E.H., Wenk, H-R. & Burlini, L., 2003. Physical properties of rocks and other geomaterials, a special volume to honour Professor H. Kern, *Tectonophysics,* **370,** 1–311.

March, A., 1932. Mathematische Theorie der Regelung nach der Korngestalt bei affiner Deformation, *Zeitschrift für Kristallographie,* **81,** 285–298.

McSkimin, H.J., Andreatch, P. Jr. & Thurnston, R.N., 1965. Elastic moduli of quartz versus hydrostatic pressure at 25° and −195.8°C, *J. Appl. Phys.,* **36,** 1624–1632.

Means, W.D., Williams, P.F. & Hobbs, B.E., 1984. Incremental deformation and fabric development in a KCl/mica mixture, *J. Struct. Geol.,* **6,** 391–398.

Parnell, J., 1992. Hydrocarbon potential of Northern Ireland; Part III, Reservoir potential of the Permo-Triassic, *Journal of Petroleum Geology,* **15,** 51–70.

Peselnick, L., Nicolas, A. & Stevenson, P.R., 1974. Velocity anisotropy in a mantle peridotite from the Ivrea Zone: Application to upper mantle anisotropy, *J. geophys. Res.,* **79,** 1175–1182.

Pettijohn, F.J., 1975. *Sedimentary rocks,* 3rd edn, pp. 628, Harper and Row, New York.

Ponte Castaneda, P. & Willis, J.R., 1995. The effect of spatial distribution on the effective behaviour of composite materials and cracked media, *Journal of the Mechanics and Physics of Solids,* **43,** 1919–1951.

Prior, D.J. & Sims, A., 1986. Quartz crystallographic fabrics of undeformed sandstones. Tectonic Studies Group, Programme and Abstracts, 17th Annual Meeting, 14–18 December, Hull, **17,** 44.

Prior, D.J. *et al.,* 1999. The application of electron backscatter diffraction and orientation contrast imaging in the SEM to textural problems in rocks, *American Mineralogist,* **84,** 1741–1759.

Reuss, A., 1929. Berechnung der Fließgrenze von Mischkristallen auf Grund der Plastizitätsbedingungen fur Einkristalle, *Zeitschrift für Angewandte Mathematik und Mechanik,* **9,** 49–58.

Sayers, C.M., 1994. The elastic anisotropy of shales, *J. geophys. Res.,* **99,** 767–774.

Schmidt, N.H. & Olesen, N.O., 1989. Computer-aided determination of crystal-lattice orientation from electron-channeling patterns in the SEM, *Canadian Mineralogist,* **27,** 15–22.

Schoenberg, M. & Muir, F., 1989. A calculus for finely layered anisotropic media, *Geophysics,* **54,** 581–589.

Seront, B., Mainprice, D. & Christensen, N.I., 1993. A determination of the three dimensional seismic properties of anorthosite: comparison between values calculated from the petrofabric and direct laboratory measurements, *J. geophys. Res.,* **98,** 2209–2221.

Thomsen, L., 1995. Elastic anisotropy due to aligned cracks in porous rock, *Geophys. Prospect.,* **43,** 805–829.

Tommasi, A., Mainprice, D., Canova, G. & Chastel, Y., 2000. Viscoplastic self-consistent and equilibrium-based modeling of olivine lattice preferred orientations: implications for the upper mantle anisotropy, *J. geophys. Res.,* **105,** 7893–7908.

Tosaya, C.A. & Nur, A., 1982. Effects of diagenesis and clays on compressional velocities in rocks, *Geophys. Res. Lett.,* **9,** 5–8.

Valcke, S.L.A., 2003. Towards the prediction of seismic anisotropy in sedimentary rocks, *MSc thesis,* University of Leeds, Leeds.

Van der Pluijm, B.A., Ho, N-C. & Peacor, D.R., 1994. High-resolution X-ray texture goniometry, *J. Struct. Geol.,* **16,** 1029–1032.

Vaughan, M.T. & Guggenheim, S., 1986. Elasticity of muscovite and its relationship to crystal structure, *J. geophys. Res.,* **91,** 4657–4664.

Venables, J.A. & Harland, C.J., 1973. Electron Backscattering Patterns– a new technique for obtaining crystallographic information in the scanning electron microscope, *Philosophical Magazine,* **27,** 1193–1200.

Vernik, L. & Nur, A., 1992. Ultrasonic velocity and anisotropy of hydrocarbon source rocks, *Geophysics,* **57,** 727–735.

Voigt, W., 1928. *Lehrbuch der Kristallphysik: mit Ausschluss der Kristalloptik,* pp. 978, B.G. Teubner, Leipzig.

Wang, Z., 2002. Seismic anisotropy in sedimentary rocks, part 2: Laboratory data, *Geophysics,* **67,** 1423–1440.

Wendt, A.S., Bayuk, I.O., Covey-Crump, S.J., Wirth, R. & Lloyd, G.E., 2003. An experimental and numerical study of the microstructural parameters contributing to the seismic anisotropy of rocks, *J. geophys. Res.,* **108,** 2365, doi:10.1029/2002JB001915.

Wenk, H.-R., 1985. Measurement of pole figures, in *Preferred orientation in deformed metals and rocks; an introduction to modern texture analysis,* pp. 11–47, ed. Wenk, H-R., Academic Press, Orlando.

Worden, R.N. & Rushton, J.C., 1992. Diagenetic K-feldspar textures; a TEM study and model for diagenetic feldspar growth, *Journal of Sedimentary Petrology,* **5,** 779–789.